Spectral analysis of Fe oxidation in the early stages of weathering and soil formation

Sánchez-Marañón, M. [a], Molinero-García, A. [a,*], Delgado, R.[a], García del Moral, L.F.[b], Martín-García, J.M.[a]

[a] Departamento de Edafología y Química Agrícola, Universidad de Granada, 18071 Granada, Spain

[b] Departamento de Fisiología Vegetal, Universidad de Granada, 18071 Granada, Spain

[*] Corresponding author.

Abstract

Chemical weathering involves the loss of elements and the oxidation of Fe. Using visible and near-infrared spectroscopy, we investigated Fe oxidation at the beginning of weathering to form a soil. Rock (mica-schist) and overlying soil (Leptosol) samples of the gravel, fine earth, coarse sand, fine sand, silt, and clay fractions (n = 69) were collected at four sites (S1-S4) of the Sierra Nevada Mountains (SE Spain). Continuum-removed spectra of the rock samples showed absorption bands near 380 and 480 nm due to octahedral Fe^{3+} electronic transitions, a multi-band absorption from 600-2100 dominated by strongly absorbing Fe^{2+} bands, as well as Al-OH and Fe-OH bands in the 2200-2500 nm region. The main change in the soil, progressively towards the smaller fraction size, was growing intensity of the bands at 380 and 480 nm as the multi-band absorption decreased, mainly near 900 nm (r = -0.78). This spectral change indicates a progressive release and oxidation of Fe from rock to the soil clay fraction. The second derivative of *K/S* in the visible range confirmed the decrease of Fe^{2+} (600 nm) and increase of Fe^{3+} as yellowish Fe oxides (420 and 480 nm) and reddish hematite (540

nm) from rock to clay. The reddish hematite resulting by weathering can also be differentiated from rock-forming hematite (520 and 560 nm). The consequent CIELAB color change in h_{ab} and C^*_{ab} was an even more consistent index of the weathering than were the chemical indices. In short, spectral and color measurements prove useful for characterizing the early stages of weathering and soil formation when the oxidation is the dominant process.

Keywords

Fe content; Oxidation state; Chemical weathering; VNIR spectroscopy; CIELAB color.

1. Introduction

Chemical weathering breaks down rocks to form soils. The change can be very slight and involve nothing more than the oxidation state of Fe, or it can be quite intense and result in the massive leaching of the more soluble components to produce new minerals (White, 2003; Yu and Hunt, 2018). A wide range of research interests in soil-weathering relationships includes the effect of weathering factors on soil development

and components (Martín-García et al., 2020; Belyazid et al., 2022), alterations in soil fertility by human influences on weathering (Brosens et al., 2021; Huang et al., 2021), soil contamination by weathering (Klaes et al., 2022), and weathering control in soil-carbon storage (Slessarev et al., 2022). All these studies, however, focus on the pedogenetic consequences of long-term weathering. Perhaps because chemical weathering is perceived as a slow process, little is known about the early stages of weathering and soil formation. Only a few studies have shown the depletion of rock-forming minerals (Mavris et al., 2010) and the mineral formation and transformation in the clay-size fraction (Mavris et al., 2011) when the soil, or material beginning to become a soil, still closely resembles rock. These researchers have indicated that weathering may be even faster in these initial phases because the transformation reactions are kinetically favored in fresh minerals, whereas other authors have reported that the breakdown decreases with the time that the mineral spends in the weathering environment (West et al., 2005; Egli and Mirabella, 2021).

Mass changes of elements, isotopes, or mineral abundance determined from either solid-state or solute compositions, defined as weathering rates (White and Buss, 2014), as well as changes in the molar ratios of bulk major element oxides, called chemical-weathering indices (Babechuk et al., 2014; Heidari et al., 2022), are commonly used for characterizing the intensity of weathering from fresh rock to topsoil. In this way, however, measurable weathering is limited to soils where bases and silica have been significantly depleted (Anderson et al., 2002). In addition, soil-forming processes typically disrupt isovolumetric weathering and absorbed ions as well as organic matter are ubiquitous in soil horizons, all of which may skew weathering rates and indices in soils (Price and Velbel, 2003). Given that much of the chemical and mineralogical information involved in the weathering analysis has been shown to be related to the

spectral reflectance (Liu et al., 2021), spectroscopic techniques are also currently being used to evaluate pedogenetic alterations (Demattê and Terra, 2014; Zhao et al., 2018) and develop predictive models of chemical weathering indices in soils (Mohanty et al., 2016).

Diffuse reflectance spectroscopy in the visible and near-infrared wavelength region (VNIR) provides distinctive absorption bands for Fe-bearing minerals (Bishop, 2019), both those that form rocks and those resulting from weathering. Features due to Fe appear mainly within the range of 350 to 1200 nm caused by electronic transitions from crystal field theory, metal-to-metal intervalence charge transfers, and ligand-to-metal charge transfers (Sherman and Waite 1985; Sherman and Vergo, 1988; Burns, 1993). Vibrational bands of OH groups combined with Fe also occur from 2300 to 2500 nm (Bishop et al., 2008; Mulder et al., 2013; Fang et al., 2018). With the help of physical and mathematical tools to enhance band resolutions and calculate color parameters, it might be possible to accurately identify and quantify Fe-bearing minerals (Scheinost and Schwertmann, 1999; Sánchez-Marañón et al., 2015; Hassani et al., 2017). This analysis, however, becomes complex in mineral mixtures due not only to overlapping Fe bands from different minerals, where Fe can also have a different oxidation state, but also to the variation in the band positions (i.e. different wavelengths) for the same mineral influenced by slight changes in the chemistry, structure, and crystal size (Scheinost et al., 1999; Cuadros et al., 2020).

Since almost no rock is free of Fe (51 g kg^{-1} Fe in the earth's crust), oxidation is common in weathering. This consists in the release of Fe, mostly Fe^{2+}, which under aerobic conditions is oxidized and, together with the strong tendency of Fe^{3+} to hydrolyze, leads to the oxidative-hydrolytic formation of oxides, hydroxides, or oxyhydroxides of Fe^{3+}, collectively called Fe oxides for short (Schwertmann, 1993;

Makiel et al., 2022). These products give the altered material the characteristic yellowish to reddish color, which indicates that chemical weathering has occurred, but we wondered whether a VNIR spectral analysis could document the oxidation process from the beginning of soil formation. The challenge is to spectrally record the change from Fe^{2+} to Fe^{3+} in milled mineral mixtures, which we will try to achieve by analyzing particle-size fractions. Given that any particle fraction can weather in only one direction—i.e. to a smaller size fraction—an interpretation of the reflectance spectra of rock, gravel, sand, silt, and clay is expected to characterize the progression of the Fe absorption bands during weathering. So far, the spectroscopic perspective of soil weathering is poorly understood and limited to soils of moderate to high weathering intensity (Demattê and Terra, 2014; Mohanty et al., 2016; Liu et al., 2021), lacking case studies with less-weathered soils. Therefore, the main objective of the present study was to investigate the spectral changes due to weathering from rock to clay in the initial stages of soil formation, paying particular attention to the oxidation process.

2. Material and methods

2.1. Sample collection and preparation

Following previous soil surveys (Sánchez-Marañón et al., 2002; Martín-García et al., 2004), a field judgment sampling was performed along an elevational gradient in the Sierra Nevada mountains (SE-Spain), looking for soil sites in rocky outcrops of mica-schists. We selected four sites at elevations of 1250 m (S1), 1900 m (S2), 2400 m (S3), and 3100 m (S4), respectively, all with similar slope (30-50%), orientation (N-NE), and vegetation (mainly *Festuca indigesta* Boiss). The climate was high-mountain Mediterranean with hot, dry summers and cold, damp winters with three-quarters of the precipitation falling as snow. The mean annual temperature and precipitation range were, respectively, from about 11°C and 698 mm at 1250 m to 0°C and 1314 mm at

3100 m. A soil in S1, S2, and S4 and two nearby soils in S3 (S3-1 and S3-2), all forming small pockets within the rock (< 0.6 m long and < 0.3 m wide and deep), were sampled in the A, C, and R horizons after digging a pit. We also took rock samples from the outcrop.

The bulked samples of soil horizons were air-dried, crumbled, and sieved through a 2-mm screen in order to separate gravel and fine earth. Both the rocks and the gravels were washed in a sink under a continuous stream of water, and then dried and crushed in a metal mortar. After removing organic matter with H_2O_2 in a subsample of fine earth and dispersing it with sodium hexametaphosphate, the coarse sand (0.25 – 2 mm), fine sand (0.05 - 0.25 mm), silt (0.002 – 0.05 mm), and clay (< 0.002 mm) were separated by a combination of sieving and sedimentation under gravity followed by oven drying at 105ºC (Sánchez-Marañón et al., 2004). For the four sampled sites, we collected a total of 69 samples: 11 crushed rocks, 8 crushed gravels, 10 fine earths, 10 coarse sands, 10 fine sands, 10 silts, and 10 clays. Subsamples were vigorously hand-ground in an agate mortar for about 10 min (Torrent and Barrón, 1993) to a soft powder.

2.2. Chemical and mineralogical analysis

All ground samples were investigated for their mineralogy with a Brucker AXS D8 Advance equipment (Cu-Kα radiation, between 3 and 70º 2θ; speed 2º min^{-1}). Mineral percentages were estimated by the intensity factor method (Martín-García et al., 1997). The major element oxides of the same samples were then determined by X-ray fluorescence (XRF) following the loss in ignition (LOI) measurement, using a compact PANalytical-model Zetium spectrometer with capacity in the elemental range from F to U. This bulk major element oxide chemistry was used to calculate three well-known chemical weathering indices: Weathering Index of Parker (WIP; Parker, 1970),

147 Chemical Index of Alteration (CIA; Nesbitt and Young, 1982), and Mafic Index of
148 Alteration (MIA; Babechuk et al., 2014).

149 In fine-earth samples (< 2 mm), following standard procedures (Klute et al., 1986;
150 Sparks et al., 1996), the particle-size distribution was analyzed by sieving (sand) and by
151 the pipette method (silt and clay), organic C content by dichromate oxidation, total N by
152 the Kjeldhal method, pH by potentiometry in a 1:1 soil:water suspension, and
153 equivalent $CaCO_3$ with a Bernard's calcimeter. Ammonium and sodium displacement
154 solutions were used to measure cation-exchange capacity and exchangeable bases.
155 Finally, atomic absorption spectrophotometry was used to measure the amount of
156 citrate/bicarbonate/dithionite-extractable iron (Fe_d) (Mehra and Jackson, 1960) and
157 ammonium oxalate-extractable iron (Fe_o) (McKeague and Day, 1966).

158 *2.3. Spectra acquisition and analysis*

159 The spectral reflectance of the 69 ground samples and the 20 unground coarse and fine
160 sand samples was measured in the VNIR region (350 - 2500 nm) using an ASD
161 FieldSpec Pro FR spectroradiometer (ASD Inc., Boulder, Co. USA) and a high-intensity
162 contact probe, with a 10-mm spot size and fitted with a 1500 h halogen bulb as the light
163 source. The baseline was calibrated with a Spectralon white reference circular panel (9
164 cm diameter, Labsphere, North Sutton, USA). We put 5 g of sample in a Teflon dish 2
165 cm high and 2.5 cm in diameter, gently pressing it by the weight of the contact probe
166 that also leveled the reflection surface. The reflectance measurement was repeated three
167 times per sample, lifting and then repositioning the probe over the sample, and each
168 measurement was generated in the system by arithmetic averaging of 10 records.
169 ViewSpec Pro v. 6.2 software (ASD Inc., Boulder, Co. USA) was used for
170 preprocessing these measured spectra, including splice correction and averaging, as well

as for calculating the continuum-removed spectrum, which is the reflectance spectrum divided by a convex curve (continuum) fit at the top connecting local maxima with straight-line segments (Clark et al., 1987). Its value is 1 where the convex curve and the reflectance spectrum match and < 1.0 where absorption bands occur. This normalization improves the resolution of the bands, which can be compared in depth, width, and position from a common baseline after removing reflectance differences (Grove et al., 1992; Vašát et al., 2014; Liu et al., 2021).

A spectral analysis restricted to the visible wavelength region was also carried out, for which diffuse reflectance measurements were made with a Minolta CM-2600d spectrophotometer (Minolta, Tokyo, Japan). This instrument has an illuminating/viewing geometry diffuse/8°, recording the light reflected by the sample with the specular component excluded between 360 and 740 nm at 10-nm intervals. After the sample was placed in Teflon cylindrical containers 15 mm in diameter and 5 mm deep with the upper surface open and leveled, measurements were made in triplicate placing the measuring port of our device with a target mask of 50 mm^2 directly on the surface of sample. Then, we transformed the reflectance *R* spectrum to ratio of absorption *K* to scattering *S* by the wavelength-dependent Kubelka-Munk function ($K/S = (1 - R)^2 / 2R$). Continuous *K/S* data *vs.* wavelengths were plotted in the OriginPro v. 7.5 program (OriginLab Co, MA, USA) to find the second-derivative curve. In this way, the resolution of *K/S* curves can be enhanced to find the position (minima values) and quantify the intensity of absorption bands by the difference in ordinate between the minimum and the next maximum at longer wavelengths (Scheinost et al., 1998). Finally, from the reflectance spectra, the Munsell color codes *hue*, *value*, and *chroma* under C illuminant and CIE 1931 Standard Observer (ASTM, 2008), as well as CIELAB color coordinates L^* (lightness), C^*_{ab} (chroma), and h_{ab} (hue-angle) under

196 D65 illuminant and CIE 1964 Standard Observer (CIE, 2018) were also calculated using
197 the Spectramagic program available in the management software of our device.

198 *2.4. Statistical analysis*

199 Principal-component analysis was applied to the data in order to reduce a large amount
200 of information to a small number of orthogonal dimensions in such a way that they
201 account for as much variation of the data set as possible (Mardia et al., 2020). Results
202 were displayed as biplots of vectors and soil scores representing variables and samples,
203 respectively. We also compared the data of several variables using one-way ANOVA in
204 order to determine whether there were significant differences between means according
205 to the *F*-ratio statistic, and to find which means were significantly different from others
206 by the multiple-range test of Fisher's least-significant differences. Alternatively, when
207 the assumptions for ANOVA were not met (e.g. the assumption of homoscedasticity),
208 we used the Kruskal-Wallis test to determine whether the medians differed according to
209 the *H* statistic. Correlation and regression analysis were also applied to the data. All
210 analyses were performed with Statgraphic Centurion XVI (Statpoint Technologies, Inc.,
211 Warrenton).

212 **3. Results**

213 *3.1. Chemical and mineralogical changes from rock to soil*

214 The bedrock of the four sampled sites (S1 to S4) was visually identified as mica-schist.
215 Its XRD analysis (Table 1) detected mainly mica, quartz, and chlorite, with minor
216 amounts of plagioclase, K-feldspar, hematite, goethite, and ilmenite, as well as traces of
217 amphibole. S1 was somewhat richer in mica while S4 had more chlorite and quartz,
218 with S2 and S3 having an intermediate composition. Among the major element oxides,
219 the highest contents were for SiO_2 and Al_2O_3, with Fe_2O_3 (total Fe) being the third in

220 abundance (Table 2). The three above oxides plus the volatiles lost on ignition (LOI)
221 and K_2O accounted for 95 wt.% of the rock chemistry.

222 In the soil, the composition of the gravel fraction was very similar to that of the rock.
223 However, for the overall dataset, the fine earth lost statistically significant amounts of
224 quartz and plagioclase but gained kaolinite and interstratified phases (Table 1), which is
225 consistent with the weathering of micaceous rock. MnO, CaO, P_2O_5, and LOI also
226 increased significantly in the fine earth (Table 2), attributable to the influx and
227 decomposition of organic matter in the soil, presence of some carbonate measured by
228 calcimetry, a Ca-saturated exchange complex, and presence of free Fe forms extracted
229 with dithionite (Fe_d) and oxalate (Fe_o) (Table 3). Input or relative enrichment of MnO,
230 CaO, and P_2O_5 in the soil therefore appears to have occurred concomitantly with the
231 formation of pedogenic Fe by weathering in the soil sites monitored. The elevational
232 gradient does not seem to have exerted any influence on the degree of weathering,
233 except maybe in S4 (3100 m). Its lower content and evolution of clay (Tables 1 and 3),
234 however, contrasts with the higher Fe_d and Fe_o contents.

235 After removing organic matter from the fine earth and separating coarse sand, fine sand,
236 silt, and clay, we also found smectite (2-9%) in the clay fraction. A principal-component
237 analysis showed that interstratified phases, kaolinite, smectite, and hematite + goethite
238 were more abundant in the clay samples, differentiating them compositionally from the
239 rest of samples along the first component (PC1, Fig. 1A). The chemical difference of
240 the clay samples was even more consistent (64.1% of variance explained in PC1, Fig.
241 1B), gaining MnO, LOI, CaO, P_2O_5, MgO, and Fe_2O_3. All other samples were better
242 aligned along PC2, whose lower explained variance suggests fewer compositional
243 differences between them. According to the distance between samples in PC2, the
244 differences between coarse sand, fine sand, and silt were even less notable than those

due to the sampling site. As in the rocks, the soil samples from S1 contained more mica and those from S4 more quartz and chlorite. Weathering did not eliminate the original compositional differences between sites.

The chemical weathering indices listed in Table 4 for the rock samples (WIP = 39-44, CIA = 75-79, MIA = 71-79) are consistent with the predominance of silicate minerals having a low content in CaO, MgO, Na_2O, and K_2O. The indices also had very similar values in the rock and soil fractions of each sampling site, indicating little loss of bases in the soil, which in turn signifies a very low degree of chemical weathering. In addition, the change of the indices through the fractions was not always as expected on rock-to-soil weathering (e.g. higher WIP and lower CIA and MIA in the soil clay fraction than in the rock). The mineral segregation by particle size, the entry of elements of biogenic origin, and perhaps also atmospheric inputs, as well as the ion absorption led to erroneous conclusions about the soil-weathering indices. It was not possible to make the necessary corrections, such as reducing the molar CaO to only the silicate–bound Ca (CaO*), because no other Ca mineral appeared in the XRD analysis, and thus the assumptions proved invalid. For example, when we subtracted the moles estimated from P_2O_5 from those measured in CaO , assuming the presence of apatite (CaO* = moles CaO – [(10/3) · moles P_2O_5]), negative values usually resulted, indicating that other no-apatite phosphates must be present in the samples. In short, the indices reflect the chemical composition of each particle-size fraction better than its chemical weathering.

3.2. Spectral analysis in the VNIR wavelength region

All reflectance spectra (Fig. 2) exhibited a steep absorption edge in the visible wavelengths starting at about 400 nm and ending near 600 nm. At longer wavelengths,

the reflectance did not increase further in most rock, gravel, and sand samples, while there was a shoulder of increasing reflectance up to 800 nm in the fine earth, silt, and clay curves. Absorption bands appeared near 400, 500, 700, 900, 1400, 1800, 1900, and 2200 nm. No spectrum exceeded 45% reflectance. In general, the slope of the absorption edge, the sharpness of the absorption bands and the reflectance values increased from rock to gravel, sand, fine earth, clay, and silt.

The continuum-removed spectra indicated in detail the absorption bands of the samples, regardless of their reflectance (Fig. 3). Bands around 380 and 480 nm, by far the most prominent, as well as near 900, 1410, 1800, 1910, and 2200 nm, appeared in all spectra but varied in depth (D) and width (W). Because the bands at 380 and 480 nm formed together an absorption basin, we jointly measured their width (W_{380}). In a similar way, W_{900} sometimes corresponded to the width of an isolated band near 900 nm but other times included the bands near 900, 1410, 1800, and 1910 nm, connected and forming a multi-band absorption in the central region of the spectrum (Fig. 3, S1.1). A correlation analysis (Table 5) revealed that as this multi-band absorption decreased (lower W_{900}, D_{900}, D_{1410} and D_{1800}), the bands at 380 and 480 nm increased (higher W_{380}, D_{380}, and D_{480}), with the band at 1910 nm (higher D_{1910}) also becoming progressively more intense. This applies both for the whole dataset (n = 69) and separately for each sampling site, showing the largest changes from rock, gravel, and sand samples to silt, fine earth, and clay samples of S3 (Fig. 3, S3) and the smallest in S4 (Fig. 3, S4).

Some spectra of rock, gravel, and sand also showed absorption features near 660-700 nm (Fig. 3, S1.1), which are generally also part of the multi-band absorption (Fig. 3, S2, S3 and S4). Other bands near 2250, 2280, 2325, and 2385 nm showed graphic evidence of attenuation in the clay samples (Fig. 3, S1.1 and S4.2) and inverse correlation with

293 the bands at 380 and 480 nm (Table 5), as well as a positive correlation with the band at
294 2200 nm.

295 Unground coarse- and fine-sand spectra also revealed a central multi-band absorption. It
296 includes, in addition to the bands at 1410, 1800 and 1910 nm, features near 1050 and
297 1200-1300 nm (Fig. 3, S3.1) and often a broad band centered at 1000 nm resulting from
298 a subtle doublet at 950 and 1050 nm (Fig. 3, S2.1 and S4.1). These bands lose definition
299 when grinding the samples, but in detail it is also possible to distinguish such bands
300 affected by a strong and progressive absorption along the SWIR1 detector (1001-1800
301 nm). Not only ground sands, but also many spectra of ground samples of rock, gravel,
302 and even silt, have a poorly defined band near 1050 nm connected with the band near
303 900 nm. This latter is approximately at 930-950 nm in rock samples forming part of the
304 multi-band absorption, but it loses intensity and moves until 880-890 nm in some clay
305 samples (Fig. 3, S1.1, S2.2 and S3.2). This is not the case in S4, where there was hardly
306 any variation between soil fractions for the band near 900 nm, and the multi-band
307 absorption persists in the clay samples with additional absorption features near 1250
308 and 1350 nm (Fig. 3, S4).

309 *3.3. Spectral analysis in the visible wavelength region*

310 The reflectance in the red range (600-700 nm) increased relatively with respect to that in
311 the blue (400-500 nm) and green (500-600 nm) as the size of the particle fraction
312 decreased (Fig. 4A), indicating a progressive coloration. On average for the four sites
313 sampled, with the use of Munsell notation, the rock was dark gray (3.9Y 4.1/0.9, n = 11)
314 and the soil dark grayish brown (2.5Y 4.1/1.3 in gravel, n = 8, and 0.7Y 4.3/2.4 in fine
315 earth, n = 10). Coarse sand (2.3Y 4.3/1.7, n = 10) and fine sand (2.5Y 4.4/1.9, n = 10)
316 gained only some Munsell *value* and *chroma* with respect to gravel, but the silt turned
317 grayish brown (0.5Y 5.1/2.5 n = 10) and the clay turned brown (9.8YR 4.8/3.2 n = 10).

318 Although subtle, many of these color changes expressed as CIELAB lightness (L^*),
319 chroma (C^*_{ab}), and hue-angle (h_{ab}) were statistically significant in an analysis of
320 variance (Table 6). At each of the sites sampled, a decreasing trend in h_{ab} was observed,
321 as well as an unequivocal increase of C^*_{ab} as the soil fraction was finer. The rock of S3
322 and S4 showed a slightly greener tint (higher h_{ab}) than S1 and S2, and among the clays,
323 the most and least red was, respectively, that of S3 (h_{ab} = 67.5) and S4 (h_{ab} = 74.8).

324 Seven main absorption bands which, based on the *K/S* second-derivative spectra
325 appeared near 420, 480, 520, 540, 560, 600, and 650 nm (Fig. 4B), jointly explained the
326 color of samples (Fig. 5A and 5B). The band ~420 nm, the most variable in position
327 (400-420) and sometimes (e.g. Fig. 4B, S1) containing another overlapping band at 430-
328 440 nm (additional shoulder or weak band), was the strongest and with increasing
329 intensity from rock to soil fractions. By contrast, the bands ~600 and ~650 nm appeared
330 more pronounced in rock than in soil fractions. For all other bands, the samples of S1,
331 S2, and S3 behaved differently from those of S4. The intensity of the band at ~480 nm
332 was highly correlated with that at ~420 nm in S4 (r = 0.86, P < 0.001), but not in S1,
333 S2, and S3. Furthermore, the modulations exhibited by the second-derivative spectra for
334 the rock samples at ~520 and ~560 nm persisted in the coarser soil fractions, but while
335 in S4 this region of the spectrum became a gently sloping straight line in the finer
336 fractions, in S1, S2, and especially in S3, a broad band appeared centered at ~540 nm.
337 For the entire dataset, a greater chroma (Fig. 5A) and redder hue (Fig. 5B) correlated
338 mainly with higher band intensity at ~420 and ~540 nm and lower band intensity at
339 ~600 and ~650 nm.

340 **4. Discussion**

341 The bands in the continuum-removed spectra of our samples at ~380 and ~480 nm (Fig.
342 3) could have been produced by the electron transitions of octahedrally coordinated

343 Fe^{3+}: $^6A_1 \rightarrow {}^4E$ and $2[^6A_1] \rightarrow 2[^4T_1]$ (Sherman and Waite, 1985). Although the presence
344 of some octahedral Fe^{3+} in phyllosilicates cannot be ruled out (Sánchez-Marañón et al.
345 2018), because the absorption coefficients of the Fe^{3+} transitions are much larger for Fe
346 oxides than for Fe-rich phyllosilicates (Sherman and Vergo, 1988), the progressive
347 increase in D_{380} and D_{480} from rock to clay, suggests mainly an enrichment in Fe oxides.
348 This is also supported by the strong relationship between the bands ~380 and ~480 nm
349 with a greater chroma (Fig. 5C) and redder hue-angle (lower h_{ab}, Fig. 5D).

350 The $2[^6A_1] \rightarrow 2[^4T_1]$ transition occurs in the range 479 to 499 nm for the more yellowish
351 Fe oxides, but from 521 to 565 nm for reddish hematite (Sherman and Waite, 1985;
352 Scheinost et al., 1998). Consequently, the *K/S* second-derivative spectra (Fig. 4B), by
353 distinguishing more bands in the visible region, reveal some details of the Fe oxides of
354 our samples. Yellowish Fe oxides must be present according to the band at ~480 nm,
355 usually attributed to goethite (Hassani et al., 2019; Cuadros et al., 2020) or a goethitic
356 structural component in Fe-defective hematite (Torrent and Barrón, 2003; Walter,
357 2006). Hematite also seems to be spectrally identified by weak bands at ~520 and ~560
358 nm in rock and coarser soil fractions, which become broad bands centered at ~540 nm
359 in the clay fraction of S1, S2, and S3 (Fig. 4B). This could be differentiating a primary
360 hematite from the rock and a secondary hematite formed in the soil. Spectral changes
361 indicate crystallochemical changes (Torrent and Barrón, 2003). In S4, there may be
362 hematite inherited from the rock (~520 nm), but there is no spectral band of secondary
363 hematite (~540 nm). A strong correlation in S4 of the band intensity at ~420 nm, which
364 corresponds to the $^6A_1 \rightarrow {}^4E; {}^4A_1$ transition common to all Fe oxides (Sherman and
365 Waite, 1985), with that at ~480 (r = 0.86), confirms that only yellowish Fe oxides were
366 formed in the soil of S4. Meanwhile, uncorrelated values in S1, S2, and S3 suggest that
367 yellowish Fe oxides as well as hematite contributed to the band ~420 nm. Indentations

368 at 430-440 nm (e.g. rock and gravel of S1, Fig. 4B) may result from hematite (Torrent
369 and Barrón, 2003) and band positions closer 400 nm (e.g. clay of S4, Fig. 4B) from
370 ferrihydrite (Scheinost et al., 1998).

371 To explain the final two bands of the *K/S* second-derivative spectra (~600 and ~650
372 nm), first, we should note that their intensity decreases from rock to clay (Fig. 4B) and
373 their effect on color is the opposite of the bands corresponding to secondary Fe oxides
374 (Fig. 5 A and B). In addition, although the ~650 nm band may coincide with the
375 position of another less intense transition of octahedral Fe^{3+} ($^6A_1 \rightarrow {}^4T_2$), in both Fe
376 oxides (Sherman and Waite, 1985) and Fe-bearing phyllosilicates (Sherman and Vergo,
377 1988; Sánchez-Marañón et al., 2018), this is not the case for the 600 nm band. In fact, a
378 similar band in biotite, chlorite, saponite, and montmorillonite spectra was correlated
379 with Fe^{2+} transitions (Faye, 1968; Sherman and Vergo, 1988).

380 At 600 nm, the multi-band absorption also begins in our continuum-removed spectra
381 (Fig. 3, S1-S4), containing additional Fe^{2+} footprints at ~660 and ~1050 nm attributed to
382 $Fe^{2+} \rightarrow Fe^{3+}$ charge transfer and octahedral Fe^{2+} crystal field transitions (Dyar 2002;
383 Cuadros et al., 2020). Meanwhile, the band near 900 nm, variable between 880 and 950
384 nm, could correspond both to the Fe^{3+} transition $^6A_1 \rightarrow {}^4T_1$ and the Fe^{2+} transition $^5T_2 \rightarrow$
385 ^5E (Sherman and Vergo, 1988; Scheinost et al., 1998). Bishop (2019) also stated that
386 these electronic transitions occur typically from 850-930 nm for ferric minerals and
387 from 950-1300 nm for Fe^{2+}-bearing silicates. With such possible assignments for the
388 900 nm band, and given its inverse correlation with the 380 and 480 nm bands (Fig 3,
389 Table 5), the progressive decrease in intensity and shift towards shorter wavelengths
390 from rock to clay for the 900 nm band (Fig. 3, S2.2 and S3.2) appears to be the spectral
391 response to a progressive decrease in Fe^{2+} and increase in Fe^{3+}. This is also consistent
392 with an increasingly red and chromatic coloration towards the finer soil fractions (Table

6) due to enrichment in Fe oxides. If these were the only ones influencing the 900 nm band, its intensity would have increased the greater the amount of Fe oxides (Richter et al., 2008; Demattê and Terra, 2014; Zhao et al., 2018)—just the opposite of what occurred in our samples. More features near 1300 and 1800 nm characteristic of Fe^{2+} in silicates (Klima et al., 2011; Percival et al., 2018; Zhang and Cloutis, 2021) were also present in our spectra (Fig. 3).

Other absorption features in the range 1400-2500 nm correspond mainly to overtones and combination bands from hydroxyl (e.g., 1410 nm) and water (1910 nm) vibrations. The maximum absorption at 2200 nm, as a typical combination of tones caused by Al-OH, suggests the predominance of Al-rich dioctahedral phyllosilicates. However, additional multiple bands between 2200 and 2500 nm (Fig. 3, S1.1) could indicate the presence of Fe^{3+}, Mg, and Fe^{2+} cations by partial replacement of octahedral Al in mica (Bishop et al., 2008; Cuadros et al., 2016; Fang et al., 2018; Liu et al., 2021). The band at ~2250 nm (Fig. 3, S4.2) is also typical of Fe in chlorite (Yang et al., 2019; Bishop, 2019). The attenuation of these bands in the clay fraction indicates that the Fe-OH and AlFeMg-OH vibrations have been reduced and, therefore, the phyllosilicates released Fe cations in the weathering.

The spectral interpretation thus makes the Fe oxidation evident. Although mineral mixing and grinding weaken the Fe^{2+} bands may be due to some handling-induced oxidation and/or dilution of the ferrous minerals, the multi-band absorption in the 600-2100 nm range could be the consequence of strongly absorbing Fe^{2+} absorptions. Many were assigned to electronic transitions (~660-700, ~950, ~1050 nm), while others (~600, ~1200-1300, ~1800 nm) were related in previous studies to the abundance of Fe^{2+} in silicate minerals. Fe^{2+} bands connected to and affecting vibrational bands (1410, 1910 nm) form the multi-band absorption that fades as Fe^{3+} bands (~380, ~480 nm)

intensify by weathering from rock to clay. The band at ~900 nm was influenced by both Fe^{2+} and Fe^{3+}. Consequently, the visible bands seemed to be the most suitable to evaluate spectrally in an unequivocal way the oxidation of Fe as a spectral index of weathering. The more intense the bands, the more Fe^{3+} and, therefore, the more weathering.

A consequence of the spectral changes by rock weathering is the coloration of soil materials (Fig. 5C and 5D). CIELAB color parameters can measure increasing weathering due to oxidation. Specifically, a C^*_{ab} ranking parallels an oxidation-intensity ranking in the soil-particle fractions from rock to clay (Table 6). The increase in C^*_{ab} due to the progressive formation of Fe oxides results in a more consistent way to estimate weathering than the chemical-weathering indices (Table 2). The oxidation progresses as the particle size decreases, but indices based on loss of bases present dysfunctions. Few bases in the original material and early stages of weathering, in addition to biogenic and atmospheric inputs, fractionation of minerals by size, and ion absorption in the soil, lead to indices showing no change in clay relative to rock. At our study sites, therefore, the C^*_{ab} oxidation index works better than chemical weathering indices WIP, CIA, and MIA. Not even the organic matter in fine earth hides spectral and color changes due to weathering.

The mineralogical data did show weathering in the clay fraction considering the presence of kaolinite, interstratified phases, and smectite, which were not in the original rock. However, we do not know what part of the hematite identified by XRD corresponds to weathering. It is the spectrum of the *K/S* second derivative (band at 540 nm) that shows unequivocally whether the clay contains a secondary hematite (Fig. 4B). This was the case at sites S1, S2, and S3, with the consequent decrease in h_{ab} (69.7, 68.6, and 67.5 CIELAB units, Table 6). The S3 had the most intense 540 nm band and

443 greatest redness in clay fraction due to secondary hematite; while S4, conversely, had
444 the yellowest clay (74.8 CIELAB units) with no trace of secondary hematite in its
445 spectrum (Fig. 4B). The spectral color indicated Fe oxides more immature and hydrated
446 in S4 than in S1, S2, and S3, consistent with the Fe_o:Fe_d ratios (Table 3). The h_{ab}
447 therefore distinguishes weathering environments, with higher temperature and lower
448 water activity favoring the formation of reddish hematite over yellowish Fe oxides.

449 **5. Conclusions**

450 Absorption features of Fe^{2+} and Fe^{3+} were already present in the spectra of original rock,
451 but the characteristic bands of Fe^{2+} weakened and those of Fe^{3+} strengthened in the soil
452 materials, indicating Fe oxidation.

453 Although the Fe^{2+} bands together caused strong absorption between 600 and 2100 nm,
454 the individual bands were poorly defined due to mineral mixing, grinding, and the
455 broad, rounded shape of the bands themselves, which also overlap. The sharpest band
456 appeared near 900 nm (880-950 nm) whose loss of intensity and displacement towards
457 shorter wavelengths was a spectral index of Fe oxidation in the soil materials with
458 respect to the rock. In general, the degree of oxidation gradually increased towards
459 gravel, sand, silt, and clay, which were soil fractions of increasing weathering.

460 Second derivative spectra of *K/S* in the visible wavelength range differentiated rock-
461 forming hematite (520 and 560 nm) from reddish hematite (540 nm) and yellowish Fe
462 oxides (480 nm) resulting from weathering. At the weathering sites studied, the band at
463 480 nm was invariably present in the soil materials, but when the 540 nm band also
464 appeared, it signified a change in the conditions for the formation of iron oxides or, the
465 equivalent, a different weathering environment.

From rock to clay, CIELAB h_{ab} progressively decreased (redder hue) and CIELAB C^*_{ab} increased (higher chroma) indicating a progressive gain in Fe oxide content. The spectral color changes were more systematic and consistent than other chemical changes determined by XRF. Accordingly, in the early stages of weathering and soil formation on acid rocks, the oxidation of Fe was more evident than the loss of elements and, therefore, the intensity of weathering can be better quantified by spectral analysis.

Acknowledgements

Financial support for this research came from the Spanish projects I+D+i B-CTS-20-UGR20 Junta de Andalucía-FEDER, PID2020-120481RB-100 Ministerio de Ciencia e Innovación, and UNGR15-CE-3531 Ministerio de Economía y Competitividad.

References

Anderson, S.P., Dietrich, W.E., Brimhall, Jr., G.H., 2002. Weathering profiles, mass-balance analysis, and rates of solute loss: Linkages between weathering and erosion in a small, steep catchment. GSA Bulletin 114, 1143–1158.

ASTM, 2008. Standard Practice for Specifying Color by the Munsell System. ASTM International D 1535‑08, PA.

Babechuk, M.G.,Widdowson, M., Kamber, B.S., 2014. Quantifying chemical weathering intensity and trace element release from two contrasting basalt profiles, Deccan Traps, India. Chem. Geol. 363, 56–75.

Belyazid, S., Akselsson, C., Zanchi, G., 2022. Water limitation in forest soils regulates the increase in weathering rates under climate change. Forests 13, 310. Doi:10.3390/f13020310.

Bishop, J.L., 2019. Visible and near-infrared reflectance spectroscopy of geologic materials. In: Bishop, J.L., Bell IIIJ.F., Moersch, J.E. (Eds.), Remote Compositional Analysis: Techniques for Understanding Spectroscopy, Mineralogy, and Geochemistry of Planetary Surfaces. Cambridge University Press, Cambridge, UK, pp. 68–101. (Chapter 4).

Bishop, J.L., Lane, M.D., Dyar, M.D., Brown, A.J., 2008. Reflectance and emission spectroscopy study of four groups of phyllosilicates: smectites, kaolinite-serpentines, chlorites and micas. Clay Miner. 43, 35–54.

Brosens, L., Robinet, J., Pelckmans, I., Ameijeiras-Mariño, Y., Govers, G., Opfergelt, S. Minella, J., Vanderborght, J., 2021. Have land use and land cover change affected soil thickness and weathering degree in a subtropical region in Southern Brazil? Insights from applied mid-infrared spectroscopy. Catena 207, 105698. https://doi.org/10.1016/j.catena.2021.105698

Burns, R.G., 1993. Mineralogical Applications of Crystal Field Theory, second ed. Cambridge University Press, Cambridge.

Clark, R.N., King, T.V.V., Gorelick, N.S., 1987. Automatic continuum analysis of reflectance spectra. In: Proceedings of the Third AIS Workshop, 2–4 June 1987. JPL Publication. vol. 87-30. JPL, Pasadena C, pp. 138–142.

CIE, 2018. Colorimetry. In: CIE (Ed.), CIE 015:2018, fourth ed. CIE Central Bureau, Vienna.

Cuadros, J., Michalski, J.R., Dekov, V., Bishop, J.L., 2016. Octahedral chemistry of 2:1 clay minerals and hydroxyl band position in the near-infrared. Application to Mars. Am. Mineral. 101, 554‑563. https://doi.org/10.2138/am-2016-5366.

Cuadros, J., Sánchez-Marañón, M, Mavris, C., Fiore, S., Bishop, J.L. Melgosa, M. 2020. Color analysis and detection of Fe minerals in multi-mineral mixtures from acid-alteration environments. Appl. Clay Sci. 193, 105677. https://doi.org/10.1016/j.clay.2020.105677

Demattê, J.A.M., Terra, F.S., 2014. Spectral pedology: A new perspective on evaluation of soils along pedogenetic alterations. Geoderma 217–218, 190–200. http://dx.doi.org/10.1016/j.geoderma.2013.11.012

Dyar, M.D., 2002. Optical and Mössbauer spectroscopy of iron in micas. In: Mottana, A., Sassi, F.P., Thompson Jr.J.B., Guggenheim, S. (Eds.), Micas: Crystal Chemistry & Metamorphic Petrology. Reviews in Mineralogy & Geochemistry. 46 Mineralogical Society of America and Accademia Nazionale dei Lincei.

Egli, M., Mirabella, A., 2021. The origin and formation of clay minerals in alpine soils. In: Hunt, A., Egli, M., Faybishenko, B. (Eds.), Hydrogeology, Chemical Weathering and Soil Formation. Geophysical Monograph Series, Wiley, pp. 121-140.

Fang, Q., Hong, H., Zhao, L., Kukolich, S., Yin, K., Wang, C., 2018. Visible and near-infrared reflectance spectroscopy for investigating soil mineralogy: A review. Journal of Spectroscopy, article ID 3168974. https://doi.org/10.1155/2018/3168974.

Faye, G.H., 1968. The optical absorption spectra of iron in six/coordinated sites in clhorite, biotite, phlogopite, and vivianite. Some aspects of pleochroism in the sheet silicates. Canadian Mineralogist 9, 403/425.

Grove, C.I., Hook, S.J., Paylor, E.D., 1992. Laboratory Reflectance Spectra of 160 Minerals, 0.4 to 2.5 Micrometers. JPL Publication, vols. 92-2. Jet Propulsion Laboratory, Pasadena, pp. 406.

Hassani, M., Saadoud, D., Chabou, M.C., Martín-Peinado, F.J., Sánchez-Marañón, M., 2017. Spectral signs of aeolian activity around a sand-dune belt in northern Algeria. Catena 182, 104175. https://doi.org/10.1016/j.catena.2019.104175.

Heidari, A., Osat, M., Konyushkova, M., 2022. Geochemical indices as efficient tools for assessing the soil weathering status in relation to soil taxonomic classes. Catena 208,105716. Doi: 10.1016/j.catena.2021.105716.

539 Huang, C., Meng, S., Tan, W., Wen, S., Li, D., Wang, B., Koopald, L.K., 2021. Regional
540 differences in mineral weathering characteristics of zonal soils under intensive
541 agriculture. Appl. Clay. Sci. 215, 106336. https://doi.org/10.1016/j.clay.2021.106336

542 IUSS Working Group WRB, 2014. World reference base for soil resources. In: International
543 Soil Classification System for Naming Soils and Creating Legends for Soil Maps.
544 World Soil Resources Reports No. 106 FAO, Rome.

545 Klaes, B., Wörner, G., Thiele-Bruhn, S., Arz, H.W., Struck, J., Dellwig, O., Groschopf, N.,
546 Lorenz, M., Wagner, J-F, Urrea, O.B., Lamy, F., Kilian, R., 2022. Element mobility
547 related to rock weathering and soil formation at the westward side of the southernmost
548 Patagonian Andes. Sci. Total Environ. 817, 15297710 doi:1016/j.scitotenv.2022.152977

549 Klima, R.L., Dyar, M.D., Pieters, C.M., 2011. Near-infrared spectra of clinopyroxenes: effects
550 of calcium content and crystal structure. Meteoritics and Planetary Science 46, 379–
551 395.

552 Klute, A. 1986. Methods of Soil Analysis: Part 1—Physical and Mineralogical Methods. Soil
553 Science Society of America, American Society of Agronomy.

554 Liu, J.-C., He, H.-P., Michalski, J., Cuadros, J., Yao, Y.-Z, Tan, W., Qin, X.-R., Li, S.-Y., Wei,
555 G.-J. 2021. Reflectance spectroscopy applied to clay mineralogy and alteration intensity
556 of a thick basaltic weathering sequence in Hainan Island, South China. Appl. Clay Sci.
557 201, 105923. https://doi.org/10.1016/j.clay.2020.105923

558 Makiel, M., Skiba, M., Kisiel, M., Maj-Szeliga, K., Błachowski, A., Szymanski, W., Salata, D.,
559 2022. Formation of iron oxyhydroxides as a result of glauconite weathering in soils of
560 temperate climate. Geoderma 416, 115780.
561 https://doi.org/10.1016/j.geoderma.2022.115780

562 Mardia, K.V., Kent, J.T., Bibby, J.M., 2000. Multivariate analysis, 7th ed. Academic Press.

563 Martín-García, J.M., Delgado, G., Sánchez-Marañón, M., Párraga, J.F., Delgado, R., 1997.
564 Nature of dioctahedral micas in Spanish red soils. Clays Miner. 31, 107-121.

565 Martín-García, J.M., Aranda, V., Gámiz, E., Bech, J., Delgado, R., 2004. Are Mediterranean
566 mountains Entisols weakly developed? The case of Orthents from Sierra Nevada
567 (Southern Spain). Geoderma 118, 115-131.

568 Martín-García, J.M., Molinero-García, A., Calero, J., Sánchez-Marañón, M., Fernádez-
569 González, M., Delgado, R., 2020. Pedogenic information from fine sand: A study in
570 Mediterranean soils. Eur. J. Soil Sci.71, 580-597.

571 Mavris, C., Egli, M., Plötze, M., Blum, J.D., Mirabella, A., Giaccai, D., Haeberli, W., 2010.
572 Initial stages of weathering and soil formation in the Morteratsch proglacial area (Upper
573 Engadine, Switzerland). Geoderma 155, 359-371.

574 Mavris, C., Plötze, M., Mirabella, A., Giaccai, D., Valboa, G., Egli, M., 2011. Clay mineral
575 evolution along a soil chronosequence in an Alpine proglacial area. Geoderma 165,
576 106-117.

577 McKeague, J.A., Day, J.H., 1966. Dithionite- and oxalate extractable Fe and Al as aids in
578 differentiating various classes of soils. Can. J. Soil Sci. 46, 13–22.

579 Mehra, O., Jackson, M., 1960. Iron oxide removal from soils and clays by a dithionite-citrate
580 system buffered with sodium bicarbonate. Clays Clay Miner. 7, 317–327.

581 Mohanty, B., Gupta, A., Das, B.S., 2016. Estimation of weathering indices using spectral
582 reflectance over visible to mid-infrared region. Geoderma 266, 111–119.
583 http://dx.doi.org/10.1016/j.geoderma.2015.11.030

584 Mulder, V.L., Plötze, M., de Bruin, S., Schaepman, M.E., Mavris, C., Kokaly, R.F., Egli, M.,
585 2013. Quantifying mineral abundances of complex mixtures by coupling spectral
586 deconvolution of SWIR spectra (2.1–2.4 μm) and regression tree analysis. Geoderma
587 207, 279–290.

588 Nesbitt, H.W., Young, G.M., 1982. Early Proterozoic climates and plate motions inferred from
589 major element chemistry of lutites. Nature 299 (5885), 715–717.
590 https://doi.org/10.1038/299715a0.

591 Parker, A., 1970. An index of weathering for silicate rocks. Geol. Mag. 10, 501–504.

592 Percival, J.B., Bosman, S.A., Potter, E.G., Peter, J.M., Laudadio, A.B., Abraham, A.C., Shiley,
593 D.A., Sherry, C., 2018. Customized spectral libraries for effective mineral exploration:
594 Mining national mineral collections. Clay Clay Miner. 66, 297-314.

595 Price, J.R., Velbel, M.A., 2003. Chemical weathering indices applied to weathering profiles
596 developed on heterogeneous felsic metamorphic parent rocks. Chem. Geol. 202 (3-4),
597 397–416. https://doi.org/10.1016/j.chemgeo.2002.11.001.

598 Richter, N., Jarmer, T., Chabrillat, S., Oyonarte, C., Hostert, P., Kaufmann, H., 2009. Free iron
599 oxide determination in Mediterranean soils using diffuse reflectance spectroscopy. Soil
600 Sci. Soc. Am. J. 73, 72–81. https://doi.org/10.2136/sssaj2008.0025.

601 Sánchez-Marañón, M., Soriano, M., Delgado, G., Delgado, R. 2002. Soil quality in
602 Mediterranean mountain environments: Effects of land use change. Soil Sci. Soc. Am. J.
603 66, 948–958.

604 Sánchez-Marañón, M., Soriano, M., Melgosa, M., Delgado, G., Delgado, R., 2004. Quantifying
605 the effects of aggregation, particle size and components on the colour of Mediterranean
606 soils. Eur. J. Soil Sci. 55, 551–565. https://doi.org/10.1111/j.1365-2389.2004.00624.x

607 Sánchez-Marañón, M., Romero-Freire, A., Martín Peinado, F.J., 2015. Soil-color changes by
608 sulfuricization induced from a pyritic surface sediment. Catena 135, 173–183.
609 https://doi.org/10.1016/j.catena.2015.07.023.

610 Sánchez-Marañón, M., Cuadros, J., Michalski, J.R., Melgosa, M., Dekov, V., 2018.
611 Identification of iron in Earth analogues of Martian phyllosilicates using visible
612 reflectance spectroscopy: spectral derivatives and color parameters. Appl. Clay Sci. 165,
613 264–276. https://doi.org/10.1016/j.clay.2018.08.016.

614 Scheinost, A.C., Chavernas, A., Barón, V., Torrent, J., 1998. Use and limitations of second
615 derivative diffuse reflectance spectroscopy in the visible to near-infrared range to
616 identify and quantify Fe oxide minerals in soils. Clay Clay Miner. 46, 528–536.

617 Scheinost, A.C., Schulze, D.G., Schwertmann, U., 1999. Diffuse reflectance spectra of Al
618 substituted goethite: a ligand field approach. Clay Clay Miner. 47, 156‑164.

619 Scheinost, A.C., Schwertmann, U., 1999. Color identification of iron oxides and
620 hydroxysulfates: use and limitations. Soil Sci. Soc. Am. J. 63, 1463–1471.

621 Schwertmann, U., 1993. Relations between iron oxides, soil color, and soil formation. In:
622 Bigham, J.M., Ciolkosz, E.J. (Eds.), Soil color. Soil Sci. Soc. Am. Spec. Pub. 31. Soil
623 Sci. Soc. Am., Madison, pp. 51–69.

Sherman, D.M., Vergo, N., 1988. Optical (diffuse reflectance) and Mössbauer spectroscopic study of nontronite and related Fe-bearing smectites. Am. Mineral. 73, 1346–1354.

Sherman, D.M., Waite, T.D., 1985. Electronic spectra of Fe^{3+} oxides and oxide hydroxides in the near IR to near UV. Am. Mineral. 70, 1262–1269.

Slessarev, E.W., Chadwick, O.A., Sokol, N.W., Nuccio, E.E., Pett-Ridge, J., 2022. Rock weathering controls the potential for soil carbon storage at a continental scale. Biogeochemistry, 157. Doi: 10.1007/s10533-021-00859-8.

Sparks, D.L., Page, A.L., Helmke, P.A., Loeppert, R.H., 1996. Methods of Soil Analysis Part 3—Chemical Methods. Soil Sci. Soc. Am., American Society of Agronomy.

Torrent, J., Barrón, V., 1993. Laboratory measurement of soil color: theory and practice. In: Bigham, J.M., Ciolkosz, E.J. (Eds.), Soil Color, Soil Sci. Soc. Am. Spec. Pub. 31. Madison, pp. 21–33.

Torrent, J., Barrón, V., 2003. The visible diffuse reflectance spectrum in relation to the color and crystal properties of hematite. Clay Clay Miner. 51, 309–317.

Vašát, R., Kodešová, R., Borůvka, L., Klement, A., Jakšík, O., Gholizadeh, A., 2014. Consideration of peak parameters derived from continuum-removed spectra to predict extractable nutrients in soils with visible and near-infrared diffuse reflectance spectroscopy (VNIR-DRS). Geoderma 232–234, 208–218. http://dx.doi.org/10.1016/j.geoderma.2014.05.012

Walter, D., 2006. Characterization of synthetic hydrous hematite pigments. Thermochim. Acta 445, 195‑199.

West, A.J., Galy, A., Bickle, M., 2005. Tectonic and climatic controls on silicate weathering. Earth and Planetary Science Letters 235, 211-228.

White, A.F., 2003. Natural weathering rates of silicate minerals. In: Holland, H.D. and Turekian, K.K. (Eds.), Treatise on Geochemistry, Vol. 5, Elsevier Science Ltd., pp. 133-168.

White, A.F, Buss, H.L., 2014. Natural weathering rates of silicate minerals. In: Drever, J.I. (Eds.), Treatise on Geochemistry, Vol. 7, Elsevier Science Ltd., pp. 115-155.

Yang, M., Han, L., Xu, Y., Ke, H., Zhou, N., Dong, H., Liu, S., Qiao, G., 2019. Near infrared spectroscopic study of trioctahedral chlorites and its remote sensing application. Open Geosci. 11:815–828.

Yu, F., Hunt, A.G., 2018. Predicting soil formation on the basis of transport-limited chemical weathering. Geomorphology 301, 21–27.

Zhang, X., Cloutis, E., 2021. Near-infrared spectra of lunar ferrous mineral mixtures. Earth and Space Science, 8, e2020EA001153. https://doi.org/10.1029/2020EA001153

Zhao, L., Honga, H., Liu, J., Fang, Q., Yao, Y., Tan, W., Yin, K., Wang, C., Chen, M. Algeo, T.J., 2018. Assessing the utility of visible-to-shortwave infrared reflectance spectroscopy for analysis of soil weathering intensity and paleoclimate reconstruction. Palaeogeography, Palaeoclimatology, Palaeoecology 512, 80–94. http://dx.doi.org/10.1016/j.palaeo.2017.07.007

666 **Figure captions**

667 **Fig. 1.** Principal component analysis. Biplots for the mineralogy (A) and bulk major
668 element oxide chemistry (B) of coarse sand (Cs), fine sand (Fs), silt (S), and clay (C)
669 samples from sites S1, S2, S3, and S4.

670 **Fig. 2.** VNIR reflectance spectra of the ground samples of rock (black), gravel (green),
671 coarse sand (dark gray), fine sand (light gray), silt (blue), clay (red), and fine earth
672 (orange) from sites S1, S2, S3, and S4. Unground coarse and fine sand spectra are also
673 shown, but offset (+, -) for clarity.

674 **Fig. 3.** Continuum-removed spectra of the ground samples of rock (black), gravel
675 (green), coarse sand (dark gray), fine sand (light gray), silt (blue), clay (red), and fine
676 earth (orange) from sites S1, S2, S3, and S4, plus some spectral details. From S1 and
677 S4: variation from rock to clay (S1.1 and S4.2). From S2, S3, and S4: comparison of
678 ground (solid line) and unground (dashed line) sands (S2.1, S3.1, and S4.1). From S2
679 and S3: change of intensity and position of the band near 900 nm in the particle
680 fractions (S2.2 and S3.2).

681 **Fig. 4.** Visible reflectance spectra (A) and second derivative of *K/S* (B) for the average
682 ground sample of rock (black), gravel (green), coarse sand (dark gray), fine sand (light
683 gray), silt (blue), clay (red), and fine earth (orange) from sites S1, S2, S3, and S4. In the
684 rock spectrum of S1, the intensity of the bands at 420 and 600 nm has been pointed out
685 as an example.

686 **Fig. 5.** Relationships between CIELAB color parameters and absorption bands. Plots of
687 observed C^*_{ab} (A) and h_{ab} (B) versus predicted values with multiple linear-regression
688 models using the intensity of the bands at 420, 480, 520, 540, 560, 600 and 650 nm in
689 the second derivative of *K/S*. Pearson's correlation coefficients are also listed. Simple
690 linear-regression models of C^*_{ab} (C) and h_{ab} (D) measured with a Minolta 2600d

691 spectrophotometer versus depth of the bands at 380 and 480 nm measured with an ASD
692 FieldSpec Pro FR spectroradiometer.
693

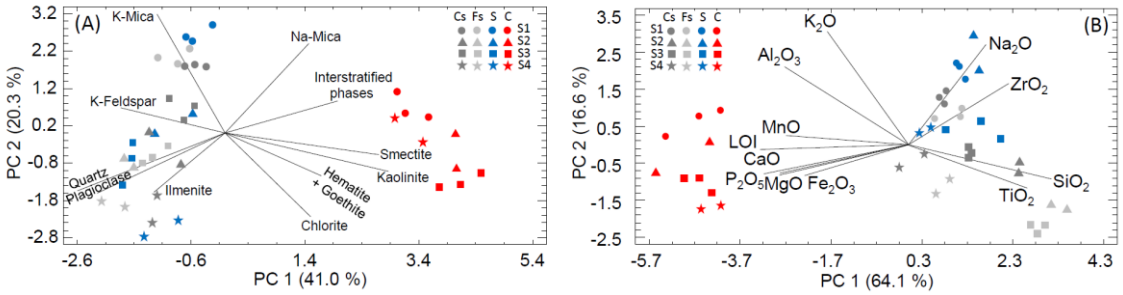

694

695 **Fig. 1.** Principal component analysis. Biplots for the mineralogy (A) and bulk major element
696 oxide chemistry (B) of coarse sand (Cs), fine sand (Fs), silt (S), and clay (C) samples from sites
697 S1, S2, S3, and S4.
698

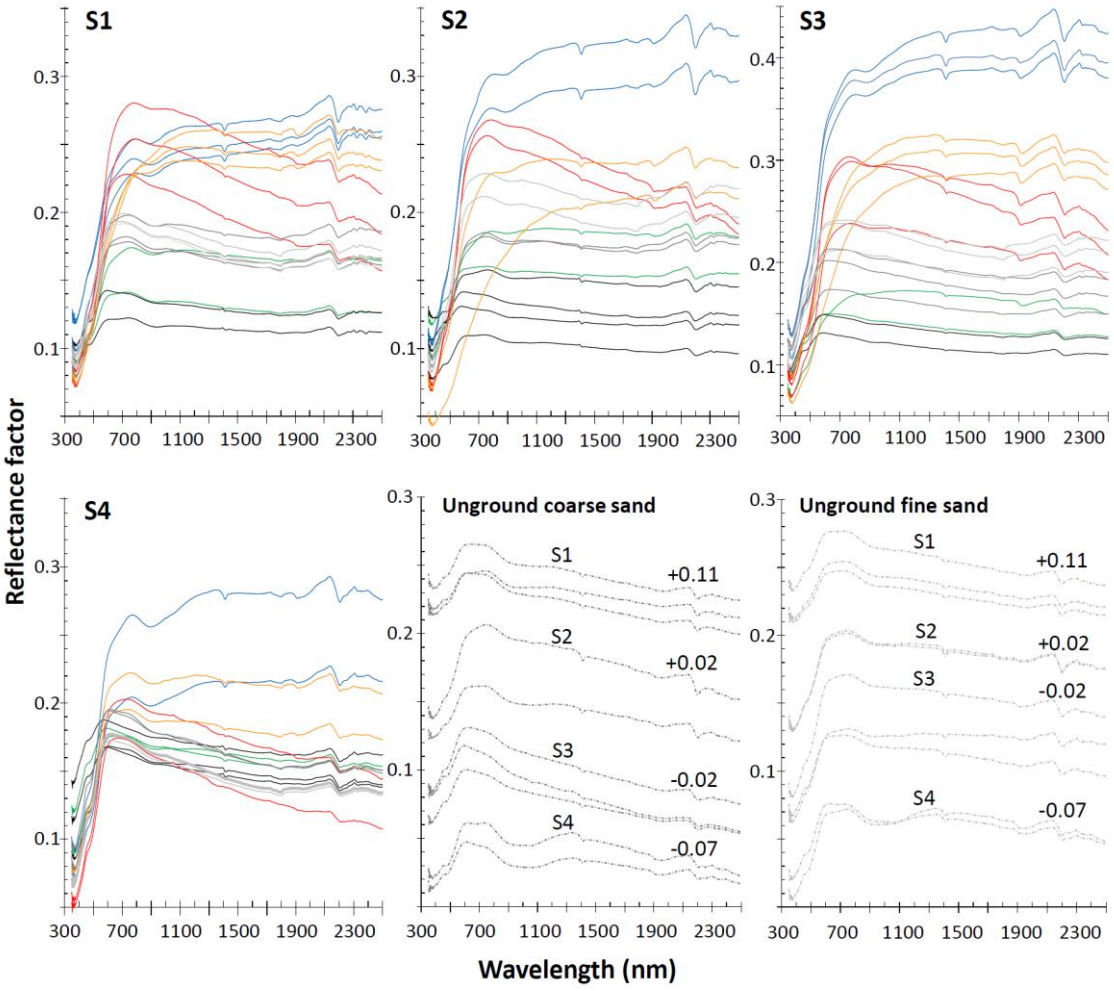

699

700 **Fig. 2.** VNIR reflectance spectra of the ground samples of rock (black), gravel (green), coarse
701 sand (dark gray), fine sand (light gray), silt (blue), clay (red), and fine earth (orange) from sites
702 S1, S2, S3, and S4. Unground coarse and fine sand spectra are also shown, but offset (+, -) for
703 clarity.
704

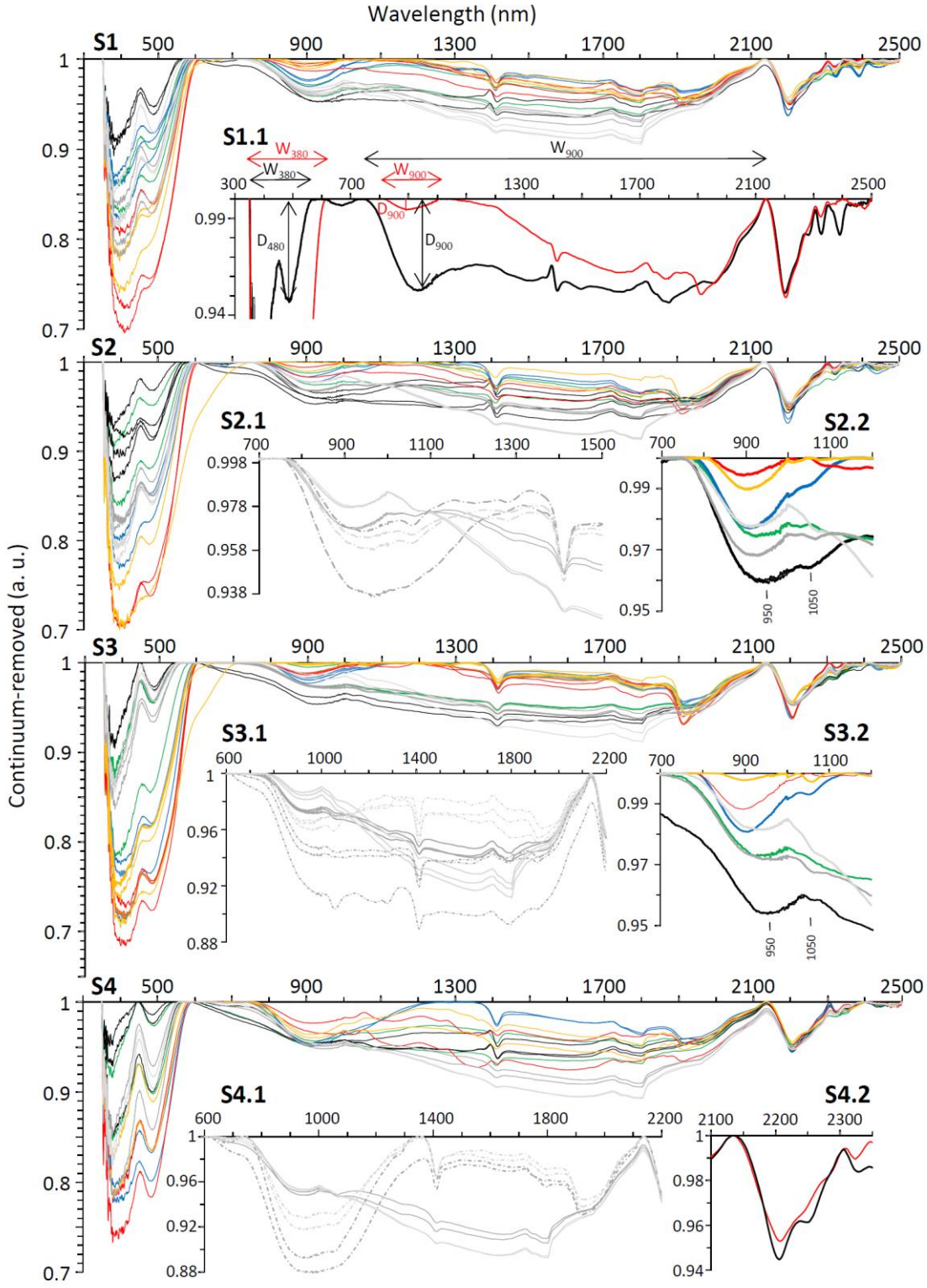

705
706 **Fig. 3.** Continuum-removed spectra of the ground samples of rock (black), gravel (green),
707 coarse sand (dark gray), fine sand (light gray), silt (blue), clay (red), and fine earth (orange)
708 from sites S1, S2, S3, and S4, plus some spectral details. From S1 and S4: variation from rock
709 to clay (S1.1 and S4.2). From S2, S3, and S4: comparison of ground (solid line) and unground
710 (dashed line) sands (S2.1, S3.1, and S4.1). From S2 and S3: change of intensity and position of
711 the band near 900 nm in the particle fractions (S2.2 and S3.2).

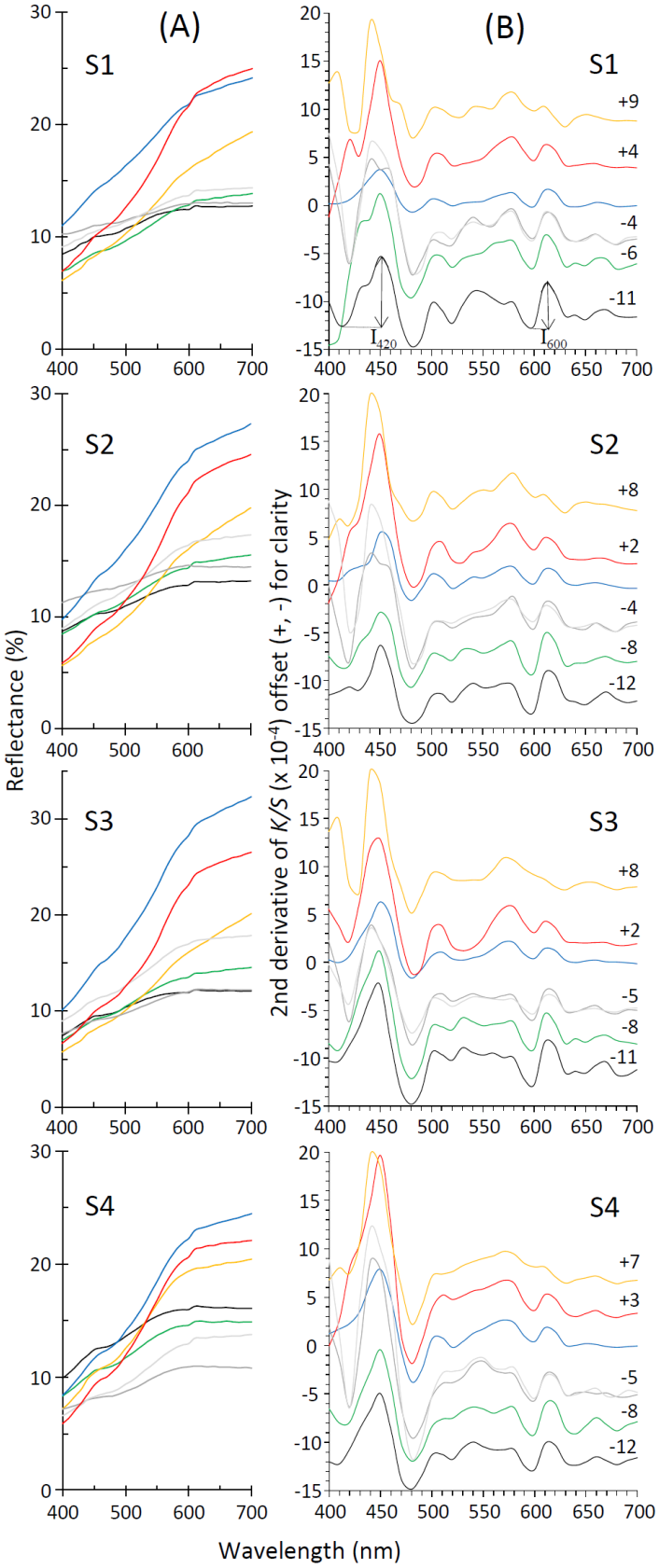

Fig. 4. Visible reflectance spectra (A) and second derivative of *K/S* (B) for the average ground sample of rock (black), gravel (green), coarse sand (dark gray), fine sand (light gray), silt (blue), clay (red), and fine earth (orange) from sites S1, S2, S3, and S4. In the rock spectrum of S1, the intensity of the bands at 420 and 600 nm has been pointed out as an example.

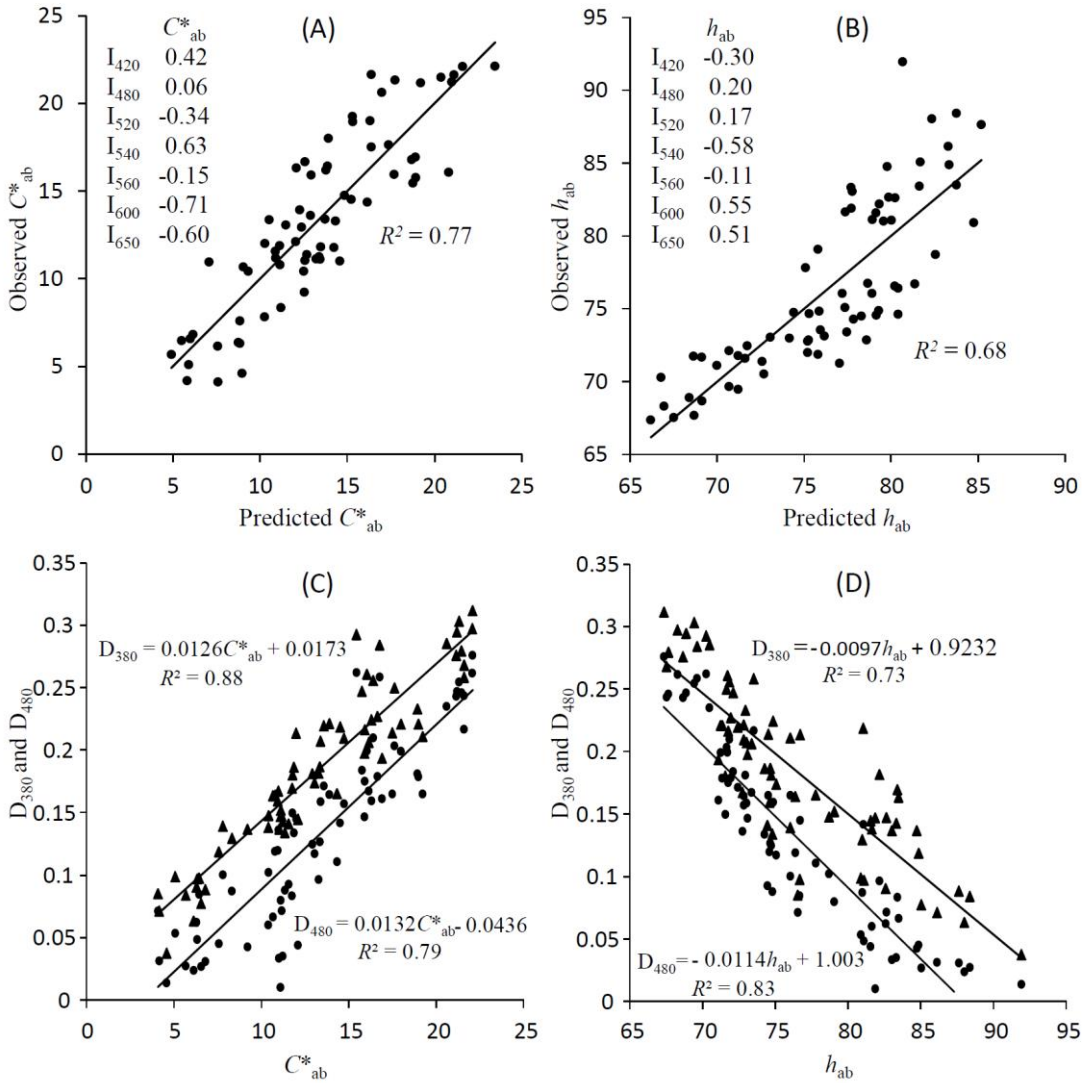

Fig. 5. Relationships between CIELAB color parameters and absorption bands. Plots of observed C^*_{ab} (A) and h_{ab} (B) versus predicted values with multiple linear-regression models using the intensity of the bands at 420, 480, 520, 540, 560, 600 and 650 nm in the second derivative of *K/S*. Pearson's correlation coefficients are also listed. Simple linear-regression models of C^*_{ab} (C) and h_{ab} (D) measured with a Minolta 2600d spectrophotometer versus depth of the bands at 380 and 480 nm measured with an ASD FieldSpec Pro FR spectroradiometer.

Table 1. Mineralogical composition (mean and standard deviation, %) of rock, gravel, and fine earth in the sampling sites S1, S2, S3, and S4. For the whole dataset (last three rows), mean values of rock, gravel, and fine earth followed by different letters are significantly different (ANOVA F-ratio > 3.5; $P < 0.05$).

Site	Sample	K-M	Na-M	Chl	Q	K-F	P	Il	Gt	Hm	K	Int
S1	Rock (n = 2)	58.2 (12.1)	13.3 (1.5)	0	18.9 (8.0)	1.8 (0.9)	4.6 (2.9)	0	1.3 (0.8)	2.2 (0.9)	0	0
	Gravel (n = 2)	59.9 (6.3)	11.9 (0.8)	0.3 (0.4)	19.85 (3.4)	1.4 (0.1)	2.1 (0.3)	0	1.9 (1.2)	2.9 (1.5)	0	0
	Fine Earth (n = 3)	65.2 (5.2)	15.2 (0.9)	1.0 (0.7)	10.9 (3.2)	1.2 (0.3)	0	0.9 (0.0)	0.7 (0.5)	1.3 (0.6)	2.0 (0.5)	1.9 (0.7)
S2	Rock (n = 4)	40.1 (11.9)	16.1 (4.2)	1.3 (1.6)	32.8 (10.9)	1.7 (0.7)	2.1 (2.4)	0.1 (0.1)	1.4 (0.4)	4.0 (2.8)	0.4 (0.5)	0
	Gravel (n = 2)	45.7 (15.3)	18.2 (4.5)	1.4 (1.0)	22.7 (11.2)	1.1 (0.9)	3.8 (5.4)	0	0.7 (0.6)	2.1 (2.1)	0.3 (0.4)	4.1 (1.9)
	Fine Earth (n = 2)	45.8 (7.1)	17.3 (1.0)	3.1 (0.3)	24.3 (3.3)	1.7 (0.1)	0	0.2 (0.0)	1.1 (0.4)	1.8 (0.5)	2.2 (1.3)	2.6 (1.3)
S3	Rock (n = 2)	49.2 (2.1)	10.3 (0.2)	3.5 (0.3)	28.7 (5.4)	0.9 (0.1)	2.8 (1.6)	0.2 (0.2)	0.4 (0.1)	2.3 (0.2)	2.0 (1.2)	0
	Gravel (n = 2)	35.8 (0.7)	11.2 (4.1)	3.8 (0.3)	37.9 (5.9)	0.9 (0.1)	3.4 (0.9)	0.2 (0.1)	0.6 (0.4)	3.4 (0.6)	2.3 (0.2)	0
	Fine Earth (n = 3)	39.1 (0.3)	11.5 (0.1)	7.0 (1.3)	25.7 (4.4)	1.7 (0.4)	0	0.2 (0.1)	1.2 (0.3)	2.6 (0.9)	6.4 (0.9)	4.5 (3.6)
S4	Rock (n = 3)	31.4 (5.4)	4.9 (1.9)	12.8 (3.0)	43.2 (3.2)	1.2 (0.2)	3.7 (2.4)	1.0 (0.9)	0.9 (0.5)	1.1 (0.3)	0	0
	Gravel (n = 2)	29.0 (1.6)	6.3 (0.5)	15.8 (3.0)	40.2 (2.3)	1.0 (0.3)	4.3 (2.1)	0.3 (0.2)	0.8 (0.6)	2.4 (0.8)	0	0
	Fine Earth (n = 2)	18.7 (4.3)	4.1 (0.2)	40.8 (4.6)	27.6 (2.7)	3.8 (2.6)	0.0	0.3 (0.1)	1.2 (0.1)	1.7 (1.1)	1.3 (0.8)	0.5 (0.1)
All	Rock (n = 11)	42.7 (12.7)	11.4 (5.4)	4.6 (5.6)	32.4a (11.0)	1.4 (0.6)	3.1a (2.2)	0.3 (0.6)	1.0 (0.6)	2.6 (2.0)	0.5a (0.9)	0a
	Gravel (n = 8)	42.6 (13.9)	11.9 (5.1)	5.3 (6.5)	30.1ab (10.9)	1.1 (0.4)	3.4a (2.4)	0.1 (0.2)	1.0 (0.8)	2.7 (1.2)	0.6a (1.0)	2.1ab (2.6)
	Fine Earth (n = 10)	44.2 (17.7)	12.3 (4.9)	11.2 (15.9)	21.4b (7.9)	2.0 (1.3)	0.0b	0.3 (0.2)	1.0 (0.4)	1.9 (0.9)	3.2b (2.3)	2.5b (2.4)

K-mica (K-M), Na-mica (Na-M), chlorite (Chl), quartz (Q), K-feldspar (K-F), plagioclase (P), ilmenite (Il), goethite (Gt), hematite (Hm), kaolinite (K), interstratified phases (Int).

Table 2. Chemical composition (mean and standard deviation, wt.%) of rock, gravel and fine earth in the sampling sites S1, S2, S3, and S4. For the whole dataset (last three rows), mean values of rock, gravel, and fine earth followed by different letters are significantly different (ANOVA F-ratio > 5.1; $P < 0.05$).

Site		SiO_2	Al_2O_3	Fe_2O_3	MnO	MgO	CaO	Na_2O	K_2O	TiO_2	P_2O_5	ZrO_2	LOI
S1	Rock (n = 2)	58.31 (1.10)	22.61 (0.60)	7.57 (0.96)	0.04 (0.01)	0.50 (0.10)	0.09 (0.01)	1.42 (0.16)	3.47 (0.26)	1.18 (0.00)	0.18 (0.01)	0.03 (0.00)	4.49 (0.00)
	Gravel (n = 2)	58.21 (0.78)	21.13 (1.20)	9.24 (0.81)	0.09 (0.01)	0.46 (0.00)	0.07 (0.02)	1.30 (0.04)	3.33 (0.35)	1.11 (0.08)	0.16 (0.01)	0.03 (0.00)	4.61 (0.11)
	Fine Earth (n = 3)	52.81 (2.62)	21.26 (1.68)	7.92 (0.48)	0.17 (0.03)	0.90 (0.27)	0.65 (0.62)	1.31 (0.06)	3.19 (0.12)	1.20 (0.07)	0.24 (0.03)	0.03 (0.00)	9.99 (4.45)
S2	Rock (n = 4)	64.43 (7.90)	18.15 (4.54)	6.82 (1.25)	0.05 (0.02)	0.63 (0.28)	0.11 (0.06)	1.51 (0.62)	2.69 (0.77)	1.14 (0.32)	0.17 (0.07)	0.04 (0.01)	4.05 (0.87)
	Gravel (n = 2)	65.28 (0.08)	17.78 (0.91)	6.71 (0.34)	0.11 (0.01)	0.72 (0.05)	0.08 (0.04)	1.28 (0.01)	2.56 (0.19)	1.11 (0.01)	0.13 (0.02)	0.04 (0.00)	4.00 (0.52)
	Fine Earth (n = 2)	60.54 (0.53)	17.09 (1.46)	7.40 (0.65)	0.15 (0.04)	0.74 (0.09)	0.39 (0.26)	1.18 (0.10)	2.46 (0.11)	1.23 (0.04)	0.23 (0.02)	0.05 (0.00)	8.42 (2.90)
S3	Rock (n = 2)	57.02 (3.11)	21.76 (1.58)	8.13 (0.83)	0.07 (0.01)	1.36 (0.12)	0.10 (0.02)	1.09 (0.09)	3.66 (0.37)	1.27 (0.06)	0.19 (0.01)	0.04 (0.00)	5.10 (0.21)
	Gravel (n = 2)	61.59 (0.41)	18.65 (0.99)	7.37 (0.24)	0.09 (0.01)	1.20 (0.08)	0.16 (0.08)	1.09 (0.08)	2.84 (0.19)	1.15 (0.08)	0.17 (0.02)	0.03 (0.00)	5.47 (1.29)
	Fine Earth (n = 3)	57.53 (1.76)	15.93 (0.48)	6.77 (0.14)	0.12 (0.01)	1.24 (0.01)	0.57 (0.09)	0.85 (0.01)	2.45 (0.05)	1.04 (0.06)	0.29 (0.03)	0.03 (0.00)	13.29 (1.15)
S4	Rock (n = 3)	64.87 (1.07)	17.71 (0.72)	6.18 (0.48)	0.07 (0.02)	1.25 (0.10)	0.45 (0.15)	0.98 (0.05)	3.18 (0.05)	1.07 (0.02)	0.11 (0.03)	0.04 (0.00)	3.90 (0.46)
	Gravel (n = 2)	60.31 (0.19)	19.21 (1.05)	8.17 (1.50)	0.08 (001)	1.39 (0.03)	0.52 (0.13)	1.20 (0.16)	3.23 (0.17)	1.11 (0.10)	0.23 (0.07)	0.04 (0.00)	4.22 (0.24)
	Fine Earth (n = 2)	56.48 (0.52)	18.06 (0.47)	11.47 (0.42)	0.08 (0.01)	1.64 (0.18)	0.84 (0.25)	1.30 (0.04)	2.50 (0.11)	1.27 (0.06)	0.55 (0.03)	0.04 (0.00)	5.80 (0.38)
All	Rock (n = 11)	62.09a (5.71)	19.49 (3.35)	7.02 (1.10)	0.06a (0.02)	0.91 (0.41)	0.20a (0.18)	1.27 (0.42)	3.14 (0.59)	1.15 (0.19)	0.16a (0.05)	0.04 (0.01)	4.28a (0.69)
	Gravel (n = 8)	61.34a (2.77)	19.19 (1.53)	7.87 (1.21)	0.09b (0.02)	0.94 (0.40)	0.20a (0.21)	1.21 (0.11)	2.99 (0.38)	1.12 (0.06)	0.17a (0.05)	0.03 (0.01)	4.57a (0.80)
	Fine Earth (n = 10)	56.50b (3.29)	18.29 (2.61)	8.18 (1.83)	0.13c (0.04)	1.12 (0.37)	0.61b (0.36)	1.14 (0.21)	2.68 (0.36)	1.17 (0.10)	0.32b (0.13)	0.04 (0.01)	9.83b (3.70)

Table 3. Soil properties at sampling sites S1, S2, S3, and S4. All soils are Leptosols (IUSS, 2015) on an R layer. Two nearby soil pockets (S3-1 and S3-2) were sampled at S3.

Sample		Depth	Gravel	Coarse sand	Fine sand	Silt	Clay	Organic C	Total N	pH	CO_3^{2-}	Ca^{2+}	Mg^{2+}	Na^+	K^+	CEC	Fe_d	Fe_o
Soil	hor.	cm	%								%	$cmol_{(+)}\,kg^{-1}$					%	
S1	Ah	0-6	39	36	18	31	15	4.6	0.4	6.8	2.0	28.5	0.9	0.4	0.1	16.3	1.5	0.2
	AC	6-14	67	28	19	41	12	1.9	0.2	6.4	1.5	13.7	2.2	0.3	0.1	9.1	1.9	0.4
	C	14-22	70	32	18	38	13	1.4	0.1	5.4	0.7	7.3	1.3	0.3	0.0	7.9	1.9	0.3
S2	Ah	0-10	49	28	23	35	14	4.7	0.3	6.3	1.2	25.6	2.3	0.7	0.3	19.0	1.6	0.5
	C	10-20	71	35	22	31	12	1.2	0.2	5.7	1.4	5.9	1.2	0.6	0.0	8.9	2.0	0.4
S3-1	Ah1	0-10	58	36	15	29	20	4.2	0.3	6.1	1.0	25.9	2.2	0.8	0.6	19.5	1.3	0.3
	Ah2	10-28	60	24	17	35	24	4.7	0.4	5.6	0.6	21.4	1.6	0.3	0.4	21.9	1.5	0.4
S3-2	Ah	0-5	51	31	18	33	19	4.6	0.3	5.8	1.1	17.8	2.3	0.6	0.4	13.9	1.4	0.3
S4	A	0-7	56	40	19	34	7	0.6	0.1	6.4	0.8	6.7	1.1	0.2	0.1	8.4	2.4	0.8
	C	7-23	71	39	25	29	6	0.8	0.1	5.9	0.3	3.3	0.7	0.6	0.1	4.2	2.2	1.0

Table 4. Pearson's correlation coefficients ($P < 0.05$) between depth (D) and width (W) of the absorption bands near 380, 480, 900, 1410, 1800, 1910, 2200, 2325, and 2385 nm in the spectra of samples taken at sites S1, S2, S3, and S4.

Site		D_{480}	W_{380}	D_{900}	D_{1410}	D_{1800}	D_{1910}	W_{900}	D_{2200}	W_{2200}	D_{2325}	D_{2385}
	D_{380}	0.98	0.76	-0.78			0.51	-0.60			-0.61	-0.59
	D_{480}		0.74	-0.78			0.56	-0.58			-0.59	-0.59
	W_{380}			-0.84	-0.60		0.66	-0.76				
S1	D_{900}				0.72	0.61	-0.89	0.85				
(n = 19)	D_{1410}					0.91	-0.87	0.77				
	D_{1800}						-0.82	0.65	-0.51			
	D_{1910}							-0.74				
	D_{2200}										0.54	0.63
	D_{2325}											0.92
	D_{380}	0.98	0.67	-0.85			0.72	-0.57			-0.56	
	D_{480}		0.73	-0.83			0.74	-0.56			-0.61	
	W_{380}			-0.70				-0.54				
S2	D_{900}				0.59		-0.79	0.78				
(n = 16)	D_{1410}					0.83	-0.71	0.79				
	D_{1800}						-0.65	0.60				
	D_{1910}							-0.79				
	W_{2200}										0.64	
	D_{380}	0.98	0.81	-0.75	-0.87	-0.81	0.95	-0.90	0.60	-0.53	-0.76	
	D_{480}		0.82	-0.65	-0.89	-0.87	0.97	-0.89	0.64	-0.52	-0.72	
	W_{380}			-0.74	-0.80	-0.74	0.76	-0.78			-0.46	
	D_{900}				0.71	0.53	-0.69	0.75			0.50	
S3	D_{1410}					0.97	-0.92	0.95			0.49	
(n = 19)	D_{1800}						-0.89	0.89	-0.49			
	D_{1910}							-0.93	0.57		-0.65	
	W_{900}								-0.49		0.56	
	D_{2200}									-0.89	-0.77	
	W_{2200}										0.83	
	D_{380}	0.90	0.94				0.61	-0.52				
	D_{480}		0.91	-0.52			0.78	-0.66				
S4	W_{380}				-0.52		0.76	-0.67				
(n = 15)	D_{900}						-0.64					
	D_{1410}					0.96	-0.65	0.67				
	D_{1800}						-0.62	0.53				
	D_{1910}							-0.54				
	D_{380}	0.95	0.74	-0.67	-0.51	-0.38	0.74	-0.69			-0.29	
	D_{480}		0.78	-0.63	-0.60	-0.45	0.79	-0.71			-0.28	
	W_{380}			-0.66	-0.60	-0.41	0.59	-0.66				
All	D_{900}				0.64	0.52	-0.65	0.70				
(n = 69)	D_{1410}					0.89	-0.77	0.80	-0.25			
	D_{1800}						-0.75	0.69	-0.37			
	D_{1910}							-0.77	0.33			
	W_{900}								-0.31		0.24	
	D_{2325}											0.32

Table 5. Mean ± standard deviation of the Weathering index of Parker (WIP), Chemical Index of Alteration (CIA), and Mafic Index of Alteration (MIA) in rock, gravel, coarse sand, fine sand, silt, clay, and fine earth at sites S1, S2, S3, and S4. For the whole dataset (last three rows), mean values of rock, gravel, coarse sand, fine sand, silt, clay, and fine earth followed by different letters are significantly different (ANOVA F-ratio > 12.1; $P < 0.05$).

Site	Index	Rock	Gravel	Coarse sand	Fine sand	Silt	Clay	Fine earth
S1	*WIP*	44.1 ± 3.43	43.6 ± 3.2	41.9 ± 0.5	40.5 ± 1.4	45.7 ± 0.7	46.6 ± 1.9	43.3 ± 0.8
	CIA	78.4 ± 1.9	78.3 ± 0.2	78.2 ± 0.2	76.9 ± 2.5	78.3 ± 0.6	78.3 ± 2.8	76.0 ± 3.9
	MIA	78.5 ± 1.4	79.4 ± 0.5	79.4 ± 0.2	77.4 ± 2.2	76.5 ± 0.9	73.4 ± 3.4	74.6 ± 4.8
S2	*WIP*	38.8 ± 10.2	35.6 ± 1.6	32.1 ± 0.6	27.0 ± 0.7	44.1 ± 1.7	41.3 ± 1.8	34.7 ± 0.9
	CIA	76.5 ± 1.4	78.0 ± 0.4	76.4 ± 0.6	75.6 ± 0.9	76.4 ± 1.7	79.8 ± 3.4	76.3 ± 2.2
	MIA	75.8 ± 0.3	76.4 ± 0.1	77.9 ± 0.53	76.8 ± 1.0	74.2 ± 1.9	74.8 ± 4.5	75.2 ± 2.7
S3	*WIP*	44.4 ± 3.6	37.8 ± 2.3	35.6 ± 0.5	25.3 ± 0.7	38.8 ± 1.1	42.0 ± 1.7	33.5 ± 0.6
	CIA	78.6 ± 0.4	78.4 ± 0.3	78.3 ± 0.3	75.9 ± 0.8	74.8 ± 1.5	78.4 ± 1.5	75.8 ± 0.2
	MIA	74.2 ± 0.3	74.1 ± 0.2	74.8 ± 0.5	73.5 ± 0.6	70.2 ± 1.4	70.7 ± 1.1	71.1 ± 0.1
S4	*WIP*	40.7 ± 1.3	43.6 ± 3.3	38.0 ± 1.2	37.0 ± 1.4	41.7 ± 0.5	35.3 ± ND	39.9 ± 0.2
	CIA	75.1 ± 1.0	75.0 ± 1.0	76.3 ± 0.0	72.6 ± 0.3	74.2 ± 0.2	82.8 ± ND	73.9 ± 1.3
	MIA	70.6 ± 1.4	71.1 ± 1.5	73.9 ± 1.0	73.0 ± 0.4	70.3 ± 0.4	75.7 ± ND	70.7 ± 1.6
All	*WIP*	41.4 ± 6.4bc	39.7 ± 3.9bc	37.3 ± 3.8b	32.6 ± 7.1a	42.5 ± 3.1c	42.6 ± 3.9c	38.0 ± 4.4b
	CIA	76.8 ± 1.8ab	77.4 ± 1.6bc	77.5 ± 1.0bc	75.5 ± 2.1a	76.0 ± 1.9ab	79.2 ± 2.5c	75.5 ± 2.2a
	MIA	74.6 ± 3.0ab	75.3 ± 3.3ab	76.6 ± 2.4b	75.2 ± 2.3ab	72.9 ± 3.1a	73.1 ± 3.1a	72.9 ± 3.2a

Table 6. Mean ± standard deviation of the CIELAB color parameters L^*, C^*_{ab}, h_{ab} in rock, gravel, coarse sand, fine sand, silt, clay, and fine earth at sites S1, S2, S3, and S4. For the whole dataset (last three rows), mean values of rock, gravel, coarse sand, fine sand, silt, clay, and fine earth followed by different letters are significantly different (ANOVA F-ratio > 16.4; $P < 0.05$).

Site	CIELAB	Rock	Gravel	Coarse sand	Fine sand	Silt	Clay	Fine earth
S1	L^*	40.8 ± 0.9	40.2 ± 1.5	42.8 ± 3.1	42.8 ± 0.5	50.9 ± 0.7	48.5 ± 0.6	43.1 ± 1.6
	C^*_{ab}	5.7 ± 0.9	9.4 ± 2.2	12.6 ± 1.6	12.5 ± 1.2	12.0 ± 0.9	19.8 ± 2.5	15.4 ± 1.3
	h_{ab}	81.7 ± 1.2	74.4 ± 2.3	74.0 ± 2.1	76.2 ± 2.5	74.8 ± 0.3	69.7 ± 1.2	72.1 ± 0.6
S2	L^*	41.2 ± 3.1	42.9 ± 1.2	42.0 ± 1.8	44.8 ± 2.1	52.0 ± 0.1	47.3 ± 0.1	42.6 ± 4.1
	C^*_{ab}	5.8 ± 2.0	8.6 ± 3.2	11.8 ± 0.1	15.5 ± 1.1	16.3 ± 0.5	21.6 ± 0.6	16.5 ± 1.5
	h_{ab}	80.1 ± 4.5	77.9 ± 4.6	72.9 ± 1.9	73.9 ± 1.4	72.5 ± 0.8	68.6 ± 0.4	71.0 ± 1.0
S3	L^*	40.1 ± 1.3	41.5 ± 0.4	45.4 ± 1.0	49.3 ± 2.0	55.1 ± 2.6	49.2 ± 1.1	43.0 ± 1.6
	C^*_{ab}	6.2 ± 0.8	9.8 ± 3.1	10.1 ± 0.8	11.5 ± 0.6	19.5 ± 0.9	21.7 ± 0.3	16.2 ± 0.5
	h_{ab}	88.0 ± 0.5	80.8 ± 5.8	83.3 ± 1.6	82.6 ± 0.9	71.6 ± 1.2	67.5 ± 0.2	71.2 ± 1.3
S4	L^*	45.7 ± 1.0	43.4 ± 0.3	45.7 ± 1.5	42.1 ± 0.2	49.9 ± 1.2	47.7 ± 1.8	47.2 ± 0.2
	C^*_{ab}	7.3 ± 3.4	8.5 ± 2.7	12.8 ± 2.4	12.5 ± 1.1	17.1 ± 1.3	20.4 ± 1.7	15.9 ± 2.2
	h_{ab}	87.3 ± 5.1	81.9 ± 4.5	81.9 ± 1.1	82.8 ± 0.9	72.3 ± 1.5	74.8 ± 1.8	76.2 ± 2.3
All	L^*	42.2 ± 2.9a	42.0 ± 1.5a	44.0 ± 2.4ab	45.0 ± 3.3b	52.2 ± 2.5c	48.3 ± 1.1d	43.8 ± 2.5ab
	C^*_{ab}	6.3 ± 2.0a	9.1 ± 2.2b	11.7 ± 1.6c	12.8 ± 1.7c	16.1 ± 3.2d	20.9 ± 1.6e	16.0 ± 1.2d
	h_{ab}	83.8 ± 5.0a	78.7 ± 4.6b	78.1 ± 5.1b	79.0 ± 4.3b	72.9 ± 1.6c	69.9 ± 2.9c	72.4 ± 2.3c